Identification and validation of a Discrete Element Model for concrete

Sébastien Hentz, Laurent Daudeville, Frédéric-Victor Donzé

To cite this version:

Sébastien Hentz, Laurent Daudeville, Frédéric-Victor Donzé. Identification and validation of a Discrete Element Model for concrete. Journal of Engineering Mechanics - ASCE, 2004, 130 (6), pp.709-719. 10.1061/(ASCE)0733-9399(2004)130:6(709) . hal-02004500

Identification and Validation of a Discrete Element Model for Concrete

Sébastien Hentz[1]; Laurent Daudeville[2]; and Frédéric V. Donzé[3]

Abstract: The use of a three-dimensional discrete element method (DEM) is proposed to study concrete structures submitted to dynamic loading. The aim of this paper is to validate the model first in the quasistatic domain, and second in dynamic compression, at the sample scale. A particular growing technique is used to set a densely packed assembly of arbitrarily sized spherical particles interacting together, representing concrete. An important difference from classical DEMs where only contact interactions are considered, is the use of an interaction range. First, the correct identification of parameters of the DEM model to simulate elastic and nonlinear deformation including damage and rupture is made through quasistatic uniaxial compression and tension tests. The influence of the packing is shown. The model produces a quantitative match of strength and deformation characteristics of concrete in terms of Young's modulus, Poisson's coefficient, and compressive and tensile strengths. Then, its validity is extended through dynamic tests. The simulations exhibit complex macroscopic behaviors of concrete, such as strain softening, fractures that arise from extensive microcracking throughout the assembly, and strain rate dependency.

Keywords: Discrete elements; Concrete; Strain rate; Dynamic loads; Models.

Introduction

The design of concrete safety structures is a big challenge for engineers; for example, some structures present in mountainous areas are dedicated to protection against natural hazards, such as avalanches, rock falls, etc. and thus may be submitted to impact loads and high deformation. Despite their geometry which is usually massive, with an extremely high fraction of reinforcement, and of course a design satisfying usual building standards, some are found to be totally damaged. This inconsistency demands further investigation and understanding of the failure mechanisms.

Different approaches have been used to model fracture of brittle geomaterials, such as concrete. Some introduce damage in the constitutive relations of the material, and most often are used for engineering purposes, whereas others deal directly with numerous microscopic cracks; the latter are often used to understand the damage mechanisms of the materials.

The use of a three-dimensional (3D) distinct element method (DEM) (Cundall and Strack 1979; Cundall 1988) is proposed here to study the fracture and the fragmentation of a complete concrete structure, which is now made feasible thanks to ever-increasing computing power. This method does not rely upon any assumption about where and how a crack or several cracks occur and propagate as the medium is naturally discontinuous, and is very well adapted to dynamic problems. Although numerous authors, (Meguro and Hakuno 1989; Potyondy et al. 1996) have used similar two-dimensional approaches to model cohesive geomaterials, few have thus modeled concrete, and even fewer have modeled complete 3D structures. This requires some modifications of the usual DEM models. Unlike continuous methods, the parameters of the material behavior model are not defined at the macroscopic scale; in addition, access to physical interaction quantities, such as friction coefficient and stiffnesses is not allowed, unlike real granular materials, for which information at the grain scale may be obtained. Therefore, a calibration of the parameters at the local scale is needed. This paper deals first with the identification of the constitutive equations parameters of the discrete element model thanks to elementary tests, such as quasistatic uniaxial compression and tension tests. Second, once parameters are known, the validation of the model will be extended through split Hopkinson pressure bar (SHPB) tests.

Discrete Element Method Model Used

The present numerical model has been implemented within the "spherical discrete element code" (SDEC) (Donzé 2000). It uses discrete spherical elements of individual radius and mass. These elements represent a polydisperse assembly with a size distribution obtained by using a particular growing technique (Donzé 2002). Once the assembly has been set, pairs of initially interacting discrete elements are identified. These interactions have been chosen to represent, as well and as simply as possible, the elastic and cohesive nature of a certain class of geomaterials, such as concrete. To do this, elastic forces with a local rupture criterion are applied between interacting elements.

---

[1] PhD Student, Univ. Joseph Fourier, Laboratoire Sols, Solides, Structures, Domaine Univ., B.P. 53, 38041 Grenoble Cedex 9 France. E-mail: sebastien.hentz@inpg.fr

[2] Professor, Univ. Joseph Fourier, Laboratoire Sols, Solides, Structures, Domaine Univ., B.P. 53, 38041 Grenoble Cedex 9 France. E-mail: laurent.daudeville@inpg.fr

[3] Professor, Univ. Joseph Fourier, Laboratoire Sols, Solides, Structures, Domaine Univ., B.P. 53, 38041 Grenoble Cedex 9 France. E-mail: frederic.donze@hmg.inpg.fr

Using the constitutive equations for each interaction, the numerical model solves the equations of motion with an algorithm similar to those used in molecular dynamics (Allen and Tildesley 1987). The explicit time integration of the laws of motion will provide the new displacement and velocity for each discrete element.

As time proceeds during the evolution of the system, changes in the packing of discrete elements may occur and new interactions be created. One of the features of this numerical model will then be to determine the interacting neighbors of a given element. This will be achieved by defining an interaction range and identifying all elements within it which are interacting. Depending on the spatial distribution of the discrete elements, two different methods are available to identify the interacting neighbors. If the distribution is rather compact with little fluctuations in size, a grid subdivision method is used (Allen and Tildesley 1987, Magnier et al. 1997). If, however, the distribution is dispersive with large size fluctuations then the previous method will be costly and a spatial sorting method is used (Müller 1996; O'Connor 1996; Magnier et al. 1997).

Interaction Range

The overall behavior of a material can be reproduced by means of this model by associating a simple constitutive law to each interaction. An interaction between elements a and b of radius R^a and R^b respectively, is defined within an interaction range γ and does not necessarily imply that two elements are in contact. Then, these elements will interact if,

$$\gamma(R^a+R^b) \geqslant D^{a,b} \tag{1}$$

where $D^{a,b}$=distance between the centroids of elements a and b and $\gamma \geqslant 1$. This is an important difference from classical DEMs which use spherical elements (Cundall and Strack 1979) where only contact interactions are considered ($\gamma=1$). This choice was made so that the method could simulate materials other than simple granular materials in particular those which involve a matrix as found in concretes. To take into account the effects of this matrix which may cement two aggregates which are not themselves in contact, the interaction range γ is set to be greater than 1 when the assembly of elements is initially built. However, this long-range interaction is limited to nearest neighbors.

The location of the interaction point is given by

$$\mathbf{x}^{a,b}=\mathbf{x}^a+(R^a-0.5((R^a+R^b)-D^{a,b})\mathbf{n} \tag{2}$$

where $\mathbf{n}$=unit vector pointing from element a to element b; and $\mathbf{x}^a$=position vector of element a.

Interaction Forces

The interaction force vector $\mathbf{F}$, which represents the action of element a on element b, may be decomposed into a normal and a shear vector $\mathbf{F}^n$ and $\mathbf{F}^s$, respectively, so that,

$$\mathbf{F}=\mathbf{F}^n+\mathbf{F}^s \tag{3}$$

where

$$\mathbf{F}^n=K^n(D_{\text{eq}}^{a,b}-D^{a,b})\mathbf{n} \tag{4}$$

where $D_{\text{eq}}^{a,b}$=equilibrium distance between the two elements a and b which was set when the interaction was created.

The normal force vector may be expressed such that it accounts for possible inelastic deformations.

The shear vector force $\mathbf{F}^s$ is computed incrementally and was given by other authors (Hart et al. 1988). The incremental force is given by

$$\Delta\mathbf{F}^s=-K^s\Delta\mathbf{U}^s \tag{5}$$

where $\Delta\mathbf{U}^s$=shear displacement vector increment between the locations of the interacting points of the two elements over a timestep Δt.

Elastic Properties

The strain energy stored in a given interaction cannot be assumed to be independent of the size of the interacting elements. Therefore, interaction stiffnesses are not identical over the sample, but follow a certain distribution. The macroscopic elastic properties, here Poisson's ratio ν, and Young's modulus E, are thus considered to be the input parameters of the model.

"Macro–micro" relations are then needed to deduce the local stiffnesses from the macroscopic elastic properties and from the size of the interacting elements. Compression tests have been run with one given sample and values linking Poisson's ratio ν, and Young's modulus E to the dimensionless values of K^s/K^n were obtained. Relations fitting these values (based on the best-fit model Liao et al. 1997) can be expressed as

$$E=\frac{D_{\text{eq}}^{a,b}}{\tilde{A}_{\text{int}}}K^n\left(\frac{0.825K^n+2.65K^s}{2.5K^n+K^s}\right) \tag{6}$$

$$\nu=\frac{K^n-K^s}{2.5K^n+K^s} \tag{7}$$

where $\tilde{A}_{\text{int}}$=surface where the interaction is defined, with

$$\tilde{A}_{\text{int}}=\pi\cdot\min(R^a,R^b)^2 \tag{8}$$

The distribution of the local stiffnesses over the sample obtained through the use of this interaction surface is another important particularity of the SDEC model. The adequacy of the relations (6) and (7) will be discussed further.

Strength Properties

Before Rupture

A modified Mohr–Coulomb rupture criterion is used. Thus, for a given interaction, a maximum tensile strength T (with $T>0$) is given and a maximum normal force $F_{\max}^n$ is defined such that

$$F_{\max}^n=-T\tilde{A}_{\text{int}} \tag{9}$$

A maximum interaction distance $D_{\max}$ is defined such that,

$$D_{\max}=D_{\text{eq}}+(\beta+1)\left(\frac{|F_{\max}^n|}{K^n}\right) \tag{10}$$

where D_{eq}=equilibrium distance; and β=softening factor for this interaction with $\beta>0$. Note that in all these developments, the indices a and b which represented the interacting elements, have been dropped to alleviate the formulations. Two cases may occur:
1.

$$F^n<F_{\max}^n \quad \text{and} \quad D<D_{\max}\Rightarrow F^n=\frac{K^n}{\beta}(D-D_{\max}) \tag{11}$$

$$F^n<F_{\max}^n \quad \text{and} \quad D\geqslant D_{\max}\Rightarrow\begin{cases}F^n=0\\F^s=0\end{cases} \tag{12}$$

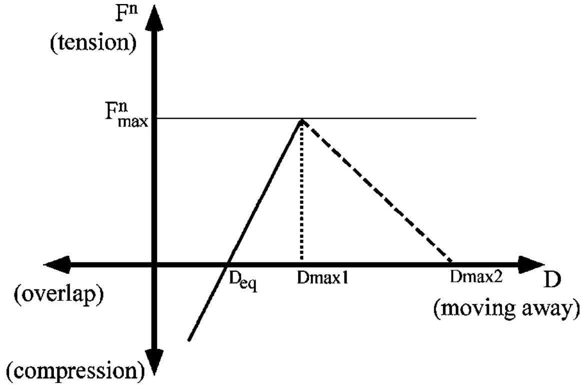

Fig. 1. Strength properties of normal force

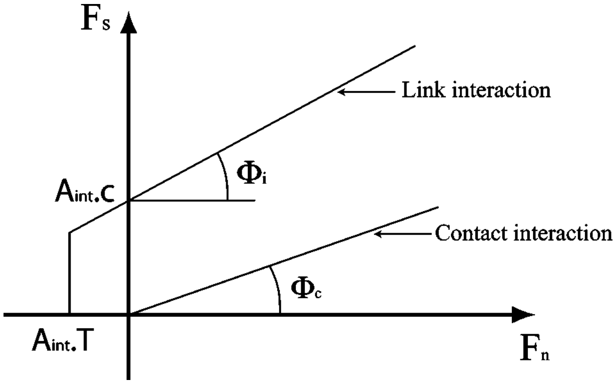

Fig. 2. Rupture criteria used in the model

The cohesive interaction is broken: Rupture occurs.

Fig. 1 summarizes the behavior of the normal force for two different values of β which illustrates the difference between a brittle elastic behavior (dotted line) and a quasibrittle behavior (i.e., presence of softening, dashed line). As long as $F^n \geqslant F^n_{\max}$ the normal force follows the solid line. As soon as $F^n < F^n_{\max}$ and depending on the value chosen for β, different paths can be followed. If $\beta \rightarrow 0$, then $D_{\max} \rightarrow D_{\max\,1}$ and rupture occurs (dotted line in Fig. 1). If $\beta = 2$ then $D_{\max} = D_{\max\,2}$ and before rupture, the normal force follows the dashed line.

However, a global softening may still be induced at the macroscopic scale while the local softening factor tends to zero if the size distribution of the elements is large enough. This is because, if there exists a large distribution of radii for the elements, then according to Eq. (9) there will be a large distribution of maximum normal forces which will in turn introduce softening effects (Herrmann et al. 1989). Therefore, some caution must be exercised before using a local softening factor.

The maximum shear force can be calculated as

$$F^s_{\max} = c\tilde{A}_{\text{int}} + F^n \tan \phi_i \tag{13}$$

where c=cohesion; and ϕ_i="internal" friction angle. If the absolute value of the shear force is

$$|F^s| = (\mathbf{F}^s \cdot \mathbf{F}^s)^{1/2} \tag{14}$$

which is greater than $|F^s_{\max}|$, then the shear force is reduced to the limiting value and written as

$$\mathbf{F}^s_{\text{reduced}} = \mathbf{F}^s [F^s_{\max} / |F^s|] \tag{15}$$

After Rupture

After initial interactions have broken, new ones are identified, which are not cohesive any more: They are merely "contact" interactions, and cannot undergo any tension force.

Then, a new maximum shear force can be calculated as

$$F^s_{\max} = F^n \tan \phi_c \tag{16}$$

where c=cohesion; and ϕ_c=contact friction angle, which may be different from ϕ_i, the internal friction angle. If the absolute value of the shear force is

$$|F^s| = (\mathbf{F}^s \cdot \mathbf{F}^s)^{1/2} \tag{17}$$

which is greater than $|F^s_{\max}|$, then the shear force is reduced to the limiting value and written as

$$\mathbf{F}^s_{\text{reduced}} = \mathbf{F}^s [F^s_{\max} / |F^s|] \tag{18}$$

Again, the use of $\tilde{A}_{\text{int}}$ induces a certain strength properties distribution over the sample, which is very consistent with a real material behavior.

Fig. 2 summarizes the rupture criteria used in the model.

Irreversible Deformations

The model is able to take into account the loss of rigidity due to damage after a compression phase, where irreversible deformations occur. To do so, the normal force vector may be expressed differently. The irreversibility will be initiated after a compressional phase ($D^{a,b} < D^{a,b}_{\text{eq}}$, where $D^{a,b}_{\text{eq}}$ is the equilibrium distance between the two elements a and b which was set when the interaction was created). In that case, a different loading and unloading path can be considered, using a coefficient α. $\alpha = 1$ means the unloading path is unchanged, and $\alpha \rightarrow \infty$ means that the unloading path is vertical. Fig. 3 summarizes the behavior of the normal force.

Homogenized Quantities

It was considered important to be able to look at the state of stress and strain in the specimen. The computation of a homogenized stress and strain has then been implemented within SDEC. As far as the stress is concerned, a technique based on an analogy with the continuous media has been chosen (Bardet 1997; Moreau

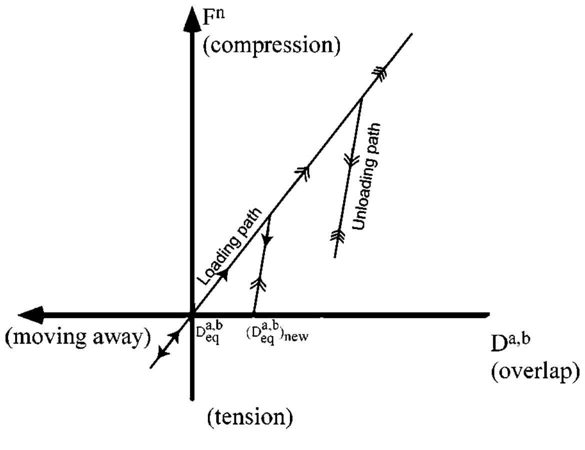

Fig. 3. Behavior of normal component of interaction force. Slope of loading path during compression is K^n; it is αK^n for unloading path during compression.

1997), the average stress σ in the volume V is defined as the weighted average of the average stress in each particle a in V, and is given by:

$$\sigma_{ij}=\frac{1}{V}\sum_{a\in V}\sum_{b\in I_a}F_i^{b\to a}R_a n_j^{ab} \tag{19}$$

where I_a=set of particle b in contact with particle a; $F^{b\to a}$=contact force of particle b on particle a; and n^{ab}=unit vector from the centroid of particle a to the contact point with particle b. The computation of the homogenized strain leads to a more complex relation: It follows the best fit method, fully described in Liao et al. (1997).

Quasistatic Simulations

Calibration of the model parameters is performed by adjusting the properties of the material represented by the assembly of discrete elements to the real geomaterial properties, a particular type of concrete. For this purpose, we have established a quasistatic uniaxial compression/traction procedure.

Sample Preparation

This is a step of particular importance, as the properties of the "discrete" material strongly depend on the packing. The samples used are standard specimens, cylinders with a height of 0.032 m and a diameter of 0.016 m. The procedure must produce isotropic packings, with a high compacity and a given size distribution. It consists in several points:

1. First, an initial set of elements, all of identical radius R, are distributed according to the most compact geometry possible (e.g., a face-centered-cubic lattice) in a cylinder shaped volume, as well as two platens, and a hollow cylinder surrounding the sample.
2. The second step introduces a certain disorder in the packing, in terms of the sample element positions, and of their radii, inside the hollow cylinder and between the bottom and top platens, which remain unchanged. This is performed thanks to an original growing technique (Donzé 2002), based on an algorithm described in Jodrey and Tory (1985); this technique is completely geometrical, unlike many others which are dynamical. It allows fine isotropy and compacity (of roughly 0.67 for the samples used). Fig. 4 shows a typical size distribution obtained.
3. The final step consists in removing the hollow cylinder around the sample in its final state.

Monitoring

The load is applied to the sample by moving the top wall downward and keeping the bottom wall at a fixed position. One difficult point is to assure the quasistatic aspect of the simulation, as the method finds the new element positions through the integration of Newton's equation, and at the same time the computational cost must stay reasonable. Therefore, attention has to be paid to the way the load is applied (low speed and low acceleration), and to the damping of the elastic waves propagating in the medium. The displacement law of the top platen consists in three phases: constant acceleration, then constant speed, then constant position. Equilibrium is checked by comparing the total forces applied by the sample to both platens, and looking at the total kinetic energy in the sample.

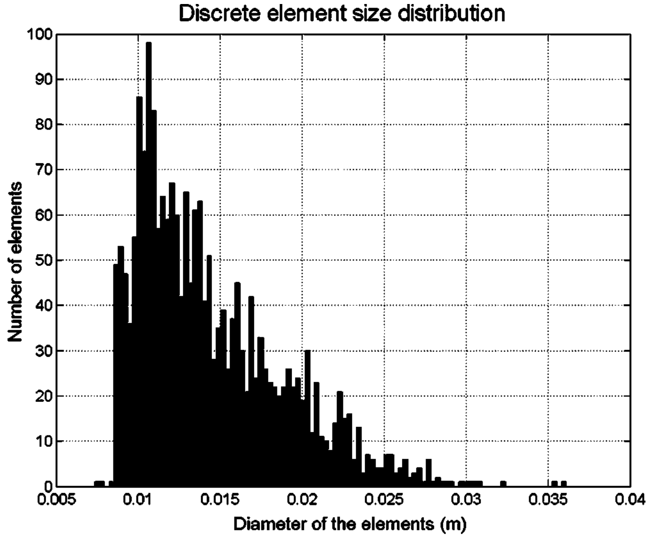

Fig. 4. Size distribution of discrete elements in the sample

Results: Elasticity

First, simulations have been run with strength properties set to very high values, so the material remains elastic. The stress is computed by dividing the total axial force applied by the plate to the sample by the surface of the sample; the axial and radial deformations are computed via geometrical measures. We deduce from these quantities Young's modulus, E and Poisson's coefficient, ν.

At this point, some remarks can be made: As usual, the DEM gives good qualitative results; the study of the homogenized stress in the medium shows a real 3D stress state and it is easy to obtain a good order of magnitude of Young's modulus and Poisson's coefficient using Eqs. (6) and (7).

However, in order to study the influence of the disorder, 20 different samples have been generated, with the same geometry, and a nearly identical size distribution (see Fig. 4), but only differing through the random aspect of their generation. They all contain roughly 2000 elements and the interaction range γ has been set to 1.55. Figs. 5 and 6 show the results. E is the sample Young's modulus, $E_m = 28$ MPa is its mean value, ν is the Poisson's coefficient, and $\nu_m = 0.252$ its mean value.

Dispersions of Young's modulus (respectively of Poisson's coefficient) are 28% (16%), and standard deviation of the ratio E/E_m (respectively ν/ν_m) are 0.07 (0.05). In addition, there is no obvious convergence of the elastic properties when the number of elements increases. Considering our objective, which is to model a complete structure, these results are somehow awkward and demand the modification of the macro–micro relations (6) and (7). This is discussed in the next section.

Energy Criterion

The strain energy E_{sd} stored in the assembly may be computed in the following way:

$$E_{sd}=\int_{\Omega_d}\mathrm{tr}(\underline{\underline{\sigma_d\cdot\varepsilon_d}})d\Omega_d=\sum_{(n,m)}\underline{F}^{n\to m}\cdot(\underline{U}^m-\underline{U}^n)$$

$$=\sum_{(n,m)}A^{nm}\cdot\underline{T}^{n\to m}\cdot(\underline{U}^m-\underline{U}^n) \tag{20}$$

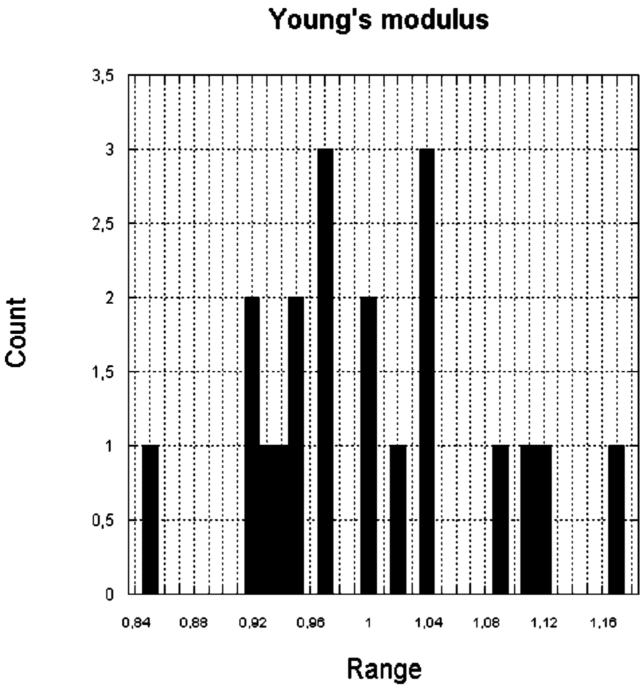

Fig. 5. Values of the ratio E/E_m

where (n,m)=interaction between the nth and the mth element; $\underline{U}^n$=displacement of the nth element; and $\underline{F}^{n\rightarrow m}$=force applied by the nth element on the mth element, proportional to the interaction surface, A^{nm}. It appears that the strain energy, and thus the elastic properties, are strongly dependent on the definition of the interaction surface. This remark leads one to plot the Young's modulus versus the total sum of the interaction surfaces in the assembly, as in Fig. 7, which shows an obvious relation between these two quantities.

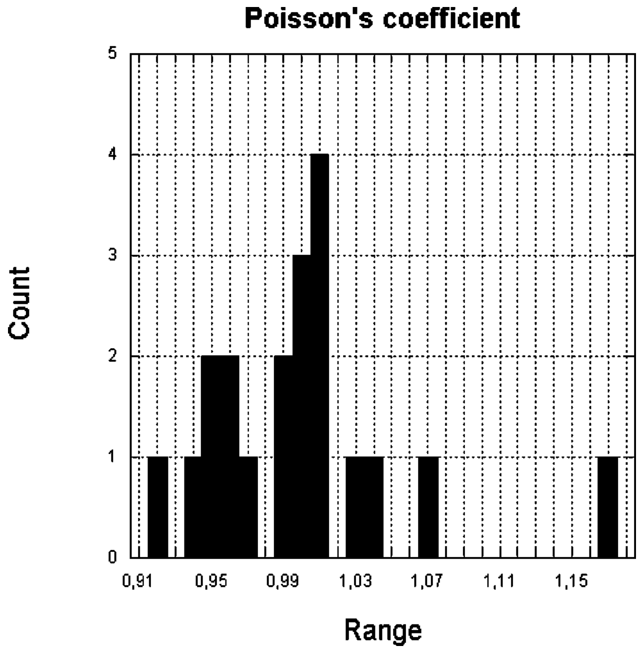

Fig. 6. Values of the ratio ν/ν_m

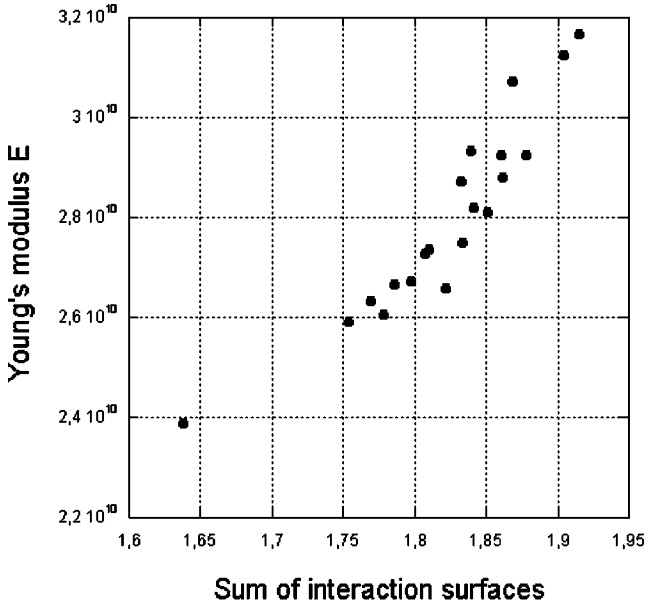

Fig. 7. Young's modulus versus the sum of the interaction surfaces

The ratio $e=E_{sc}/E_{sd}$ was computed for each assembly, where E_{sd} is the strain energy we wish to store in the real concrete sample.

It is easy to show that

$$e=\frac{E_{sc}}{E_{sd}}=\frac{E}{E_{\mathrm{app}}}\cdot\frac{S}{S_{\mathrm{app}}}\cdot\frac{\ell_{\mathrm{app}}}{\ell} \tag{21}$$

where the indice app corresponds to the apparent properties of the discrete sample.

It appears that e differs from assembly to assembly and is not equal to one. The decision was then made to use as new interaction surfaces $A^{nm'}=e\cdot A^{nm}$, and to run the same tests. Results show the new dispersions of Young's modulus (respectively of Poisson's coefficient) are 12% (10%), and standard deviation of the ratio E/E_m (respectively ν/ν_m) are 0.038 (0.03). This is an encouraging result, as dispersions are divided by roughly 2. With the energy criterion, the influence of the random aspect of the assembly generation, as well as the influence of the number, size, and local configuration of the elements, is highly reduced.

Results: Rupture

Parameters of the model are here set to study the fracture of the sample, and to obtain strength properties of a typical concrete. Properties of interest in this section are the compression and tension strengths σ_c and σ_t, and their associated strains ε_c and ε_t, as well as the fracture energy G_f. First, concrete behavior is qualitatively very well represented, and the simulations exhibit a very similar response to observations during a laboratory uniaxial compression test.

However, the high value of the ratio σ_c/σ_t for concrete, makes its behavior very specific, and has to be numerically matched. If unchanged, the SDEC model can only reach a ratio of around 3 or 4 [Huang (1999) obtained the same value with a similar model]. This is due to the fact that a single interaction between two elements does not transmit any moment: Relative rotation without sliding is free. Therefore, rotations are prevented for the following simulations, which led to a very correct ratio σ_c/σ_t around 8. Then, the use of the softening factor led to Gf

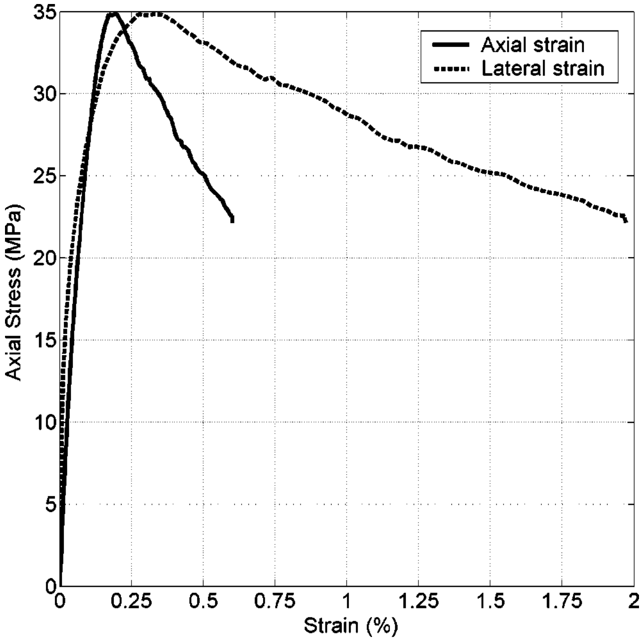

Fig. 8. Stress/strain plot in compression

$\simeq 60\,\mathrm{J\,m}^{-2}$, which is not far from typical values for concrete. Figs. 8 and 9 show one typical stress/strain plot obtained. This plot shows tendencies very similar to what can be observed on a real concrete sample.

In order to estimate how the values of interest are affected by the random aspect of the assembly generation, tests have been run with the 20 different assemblies already used in elasticity, and with the corrected interaction surfaces. Results show that dispersions of compressive strength (respectively of tension strength) are 19% (31%), and standard deviation of the ratio σ_c/σ_{cm} (respectively σ_t/σ_{tm}) are 0.047 (0.083), where σ_{cm} (respectively σ_{tm}) are the mean compression (tension) strengths, 36 MPa (4.4 MPa). Compared with the elasticity dispersions, these values are higher, but not so far from what could be obtained with real concrete failure tests, which makes these results very satisfactory.

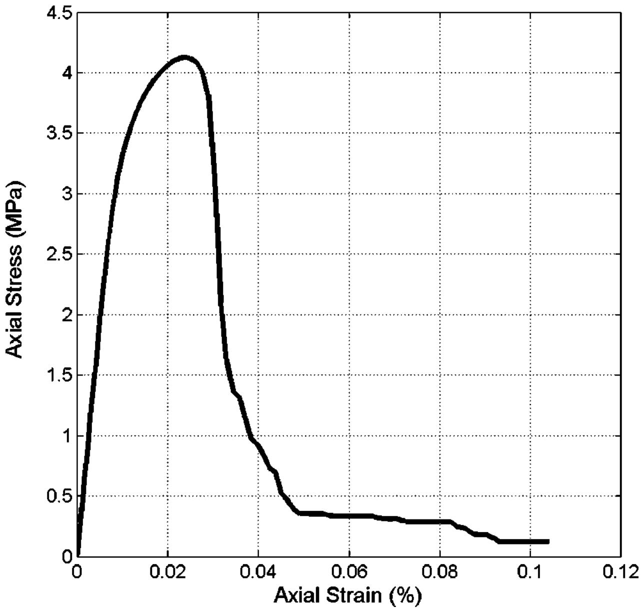

Fig. 9. Stress/strain plot in tension

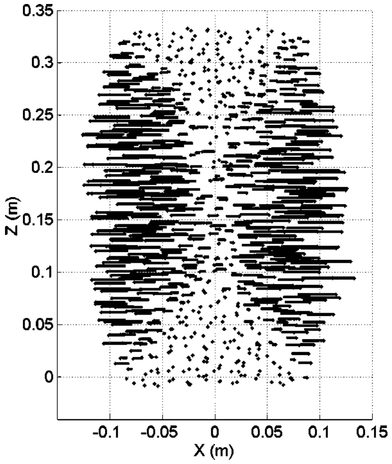

Fig. 10. Radial displacement field in an axial cut after failure in compression

In addition, failure patterns show a good match with experimental results, see Figs. 10 and 11. In compression, fretting cones appear, as the elements are "glued" to the platens, which is consistent with experimental observations. In tension, a macrocrack perpendicular to the loading direction appears, which was expected. The study of the homogenized strain shows a clear strain localization in this macrocrack, in the peak region.

Dynamic Simulations: Split Hopkinson Pressure Bar Experiments

Keeping in mind our objective, which is to model a concrete structure submitted to impact loading, it is of importance to validate the model through dynamic simulations. Now, simulations have shown that the method is able to reproduce the quasistatic behavior of concrete, the writers propose here to simulate dynamic compression tests.

Uniaxial compressive or tensile strengths of concrete increase with an increase in strain rate. At low strain rates, ($\dot{\varepsilon} < 1 s^{-1}$), this effect is relatively well explained by the presence of free water in

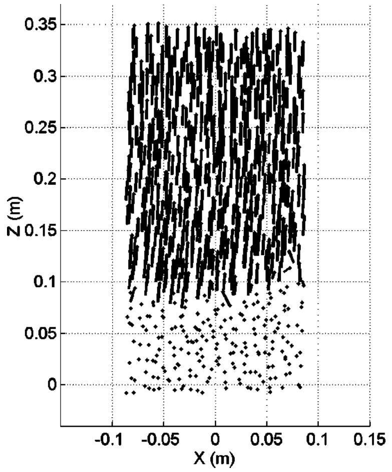

Fig. 11. Displacement field in an axial cut after failure in tension

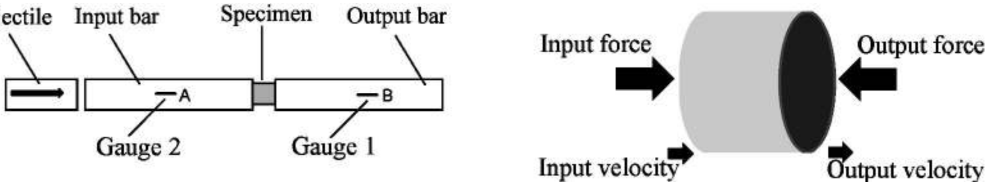

Fig. 12. Setup for split Hopkinson pressure bar experiment

the material (Rossi et al. 1992); Traction tests on dry concrete have shown no such rate effect, which confirms this assumption (Rossi et al. 1994). The rate dependence is thus well represented by a viscous model (Dubé et al. 1996; Gopalaratnam et al. 1996). At higher strain rates, $(\dot{\epsilon}>10^2\ \mathrm{s}^{-1})$, some authors (Brace and Jones 1971; Bischoff and Perry 1991) argue that inertia, producing an effective confining stress, plays a major role in the apparent and important rate dependence. Accurate information may now be obtained with SHPB tests, in terms of forces and displacements of the specimen. Donzé et al. (1999) used a similar 3D model to simulate some SHPB tests, without a reliable identification of the sample behavior. Nevertheless, this first study confirmed the inertia-based hypothesis.

Dynamic Compression

A typical SHPB experimental setup (Zhao and Gary 1996) is shown in Fig. 12. It consists in two long aligned metallic bars and a short concrete specimen between them. A projectile impacts the free end of the input bar thus leading to the development of a compressive longitudinal incident wave $\varepsilon_i(t)$. Once it arrives at the bar–specimen interface, it splits into a reflected wave $\varepsilon_r(t)$ which travels in the input bar and a transmitted wave $\varepsilon_t(t)$ which travels in the output bar. These three waves are recorded by gauges which have been cemented on each bar. They are then artificially shifted so as to record them at the bar–specimen interfaces, so that the forces and velocities measured on both faces of the specimen (Zhao and Gary 1996) are given by

$$V_{\mathrm{input}}(t)=C(\varepsilon_i(t)-\varepsilon_r(t)) \tag{22}$$

$$V_{\mathrm{output}}(t)=C\varepsilon_t(t) \tag{23}$$

$$F_{\mathrm{input}}(t)=S_B E(\varepsilon_i(t)+\varepsilon_r(t)) \tag{24}$$

$$F_{\mathrm{output}}(t)=S_B E\varepsilon_t(t) \tag{25}$$

where $C=\sqrt{E/\rho}$=celerity of the medium; E=Young's modulus; ρ is the density; and S_B=cross-sectional area of the bars.

Once these forces and velocities are obtained, a so-called three-waves formula gives the average strain rate and the average stress imposed on the specimen, so that,

$$\dot{\varepsilon}_s(t)=\frac{V_{\mathrm{output}}(t)-V_{\mathrm{input}}(t)}{l_s} \tag{26}$$

$$\sigma_s(t)=\frac{F_{\mathrm{input}}(t)+F_{\mathrm{output}}(t)}{2S_s} \tag{27}$$

where ℓ_s and S_s denote respectively the length and the cross-sectional area of the specimen.

The complete data set then consists of F_{input}, F_{output}, V_{input}, and V_{output}. If the correct constitutive behavior has been used in a model, then given one of these pairs, the other data pair should be obtained. In the following simulations, the velocities will be used as the input data and the forces will thus be computed numerically and compared to the real experimental data forces.

Experimental Data Set

SHPB tests on concrete specimens have been carried out by Gary (1990) in the framework of the "GRECO géomatériaux project" and data obtained from these different tests were made widely available.

The concrete specimens that are used are cylinders with a height of 0.036 m and a diameter of 0.036 m. The density is 2500 kg/m^3 and the average compressive wave velocity is 3865 m/s (Toutlemonde 1995).

Three loading experiments, ms2b, ms3b, and ms5b, respectively at 350 s^{-1}, 500 s^{-1}, and 700 s^{-1} strain rate have been run and for each of these runs both the input and output velocities and forces are recorded. Some problems in these recordings have to be noted: Arrival times of the output velocities vary in a large range, and so do the Young's moduli which are much lower than what was expected from the static value (Toutlemonde 1995) which is more than 30 GPa. The Young's moduli are obtained from the slopes of the stress strain curves of Fig. 13. This plot is deduced from Eqs. (26) and (27), and shows best the strain rate dependency.

Such fluctuations in the data set are not surprising when considering the very high strain rates at which these experiments are run and may come from the error bar on the applied correction of the travel times of the compressive waves, but it makes it extremely difficult to define a precise reference material that could be used in the numerical model. Despite these difficulties, local

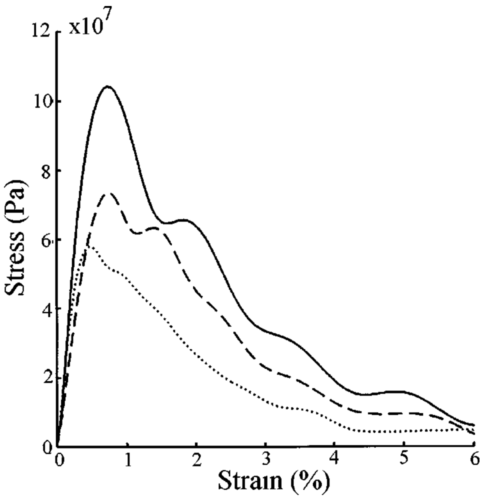

Fig. 13. Stress versus strain curves for experimental data set. Solid, dashed and dotted lines are, respectively, experiments ms5b, ms3b, and ms2b. Slopes of curves give elastic modulus.

Table 1. Local Parameter Values

Parameters	Values
γ	1.4
α	1
β	1
T (MPa)	7
c (MPa)	3.5
ϕ_i (degrees)	4
ϕ_c (degrees)	40

parameters were calibrated using the quasistatic procedure already discussed to obtain the expected concrete behavior: Density 2,500 kg/m^3, Young's modulus 30 GPa, Poisson's coefficient 0.2, compressive strength 50 MPa, and tension strength 5 MPa. Table 1 shows the values of the local parameters.

Numerical Setup

Up to 6,200 spherical discrete elements with sizes ranging from 9.10^{-4} m to 47.10^{-4} m, have been used to build the numerical concrete sample, and the shape of the size distribution is similar to Fig. 4.

The experimental input and output velocities are applied to the platens. The radial displacement values are assumed to be zero on the input and output surfaces. The resulting input and output forces are computed by summing all the forces applied on the platens. Given the experimental velocity histories, at each time step, the applied input and output velocities are updated leading to the computation of numerical force histories. No damping has been used, and rotations are still prevented.

Results

Fig. 14 shows force histories for both the experiment and the simulation at 350 s^{-1}, as well as the number of broken interactions during the simulation. The global wave form of the signal, as well as the amplitude are well reproduced, which is comforting.

In particular, the elastic phase fits very well, for both input and output phases. However, fractures arise a little too soon, and thus the amplitude of the input force is slightly too low; at the same time, the amplitude of the numerical output force exceeds that of the experiment, meaning that the material is not damaged enough. When the force is at its peak, more than one-third of the interactions have ruptured.

The oscillation amplitude of the postpeak region is slightly too low as far as the input force is concerned, but quite well reproduced for the output force. It seems then that the numerical behavior around the peak is too ductile.

At the end of the simulation, numerical and experimental samples show very similar behaviors, except in the last 30 μs. Fractures keep occurring, spreading all over the sample.

Fig. 15 shows stress/strain curves obtained for the three tests [stress and strain are deduced from the computationed forces and velocities by Eqs. (26) and (27)]. The experimental curves are very well fitted in the prepeak region, but this is less often the case after the peak, except for ms2b. The behavior seems too brittle in the last part of the simulation. Maximum amplitudes of computationed stress fits the experimental stress quite well, despite the recording problems of the tests. Fig. 16 shows the damage state of the sample for a given stress of 50 MPa in the elastic phase, for the slowest and the fastest test. As the damage increases, the color darkens. It can clearly be seen that as the strain rate increases, the extent of the damage lessens. Moreover, this damage, very diffuse, is not homogeneous and tends to propagate inwardly from the lateral free surfaces of the specimen thus forming a contact cone as seen in real experiments.

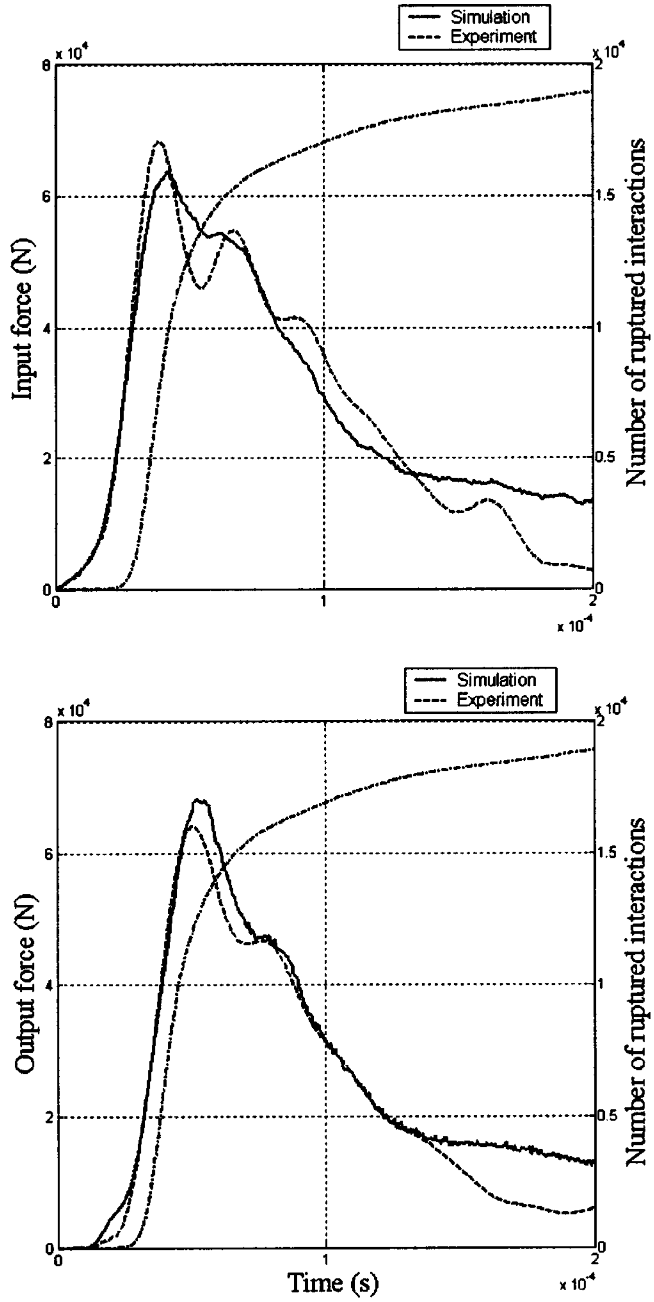

Fig. 14. Input and output forces for ms2b (350 s^{-1}). Dotted lines are original experimental curves; solid lines are computed numerical results.

The model proves able to quantitatively reproduce the increase of compressive strength with the increase of loading rate, and this, without requiring the use of viscosity in the model, or of any characteristic time. An inertia-based hypothesis, given by Janach (1976), might then explain the strain rate dependency: The compressive stress wave C in the brittle material generates a dilation in the radial direction because of the opening of cracks. Thus, the material exhibits a reduced unloading modulus in the radial direction which allows the damage zone to propagate inwardly from the free surface with an unloading velocity C_f which can be less

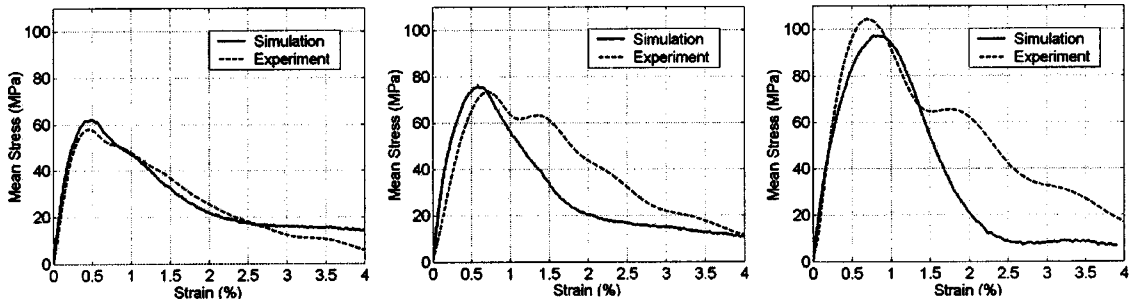

Fig. 15. From the left- to right-hand side: Stress/strain curves for ms2b, ms3b, and ms5b

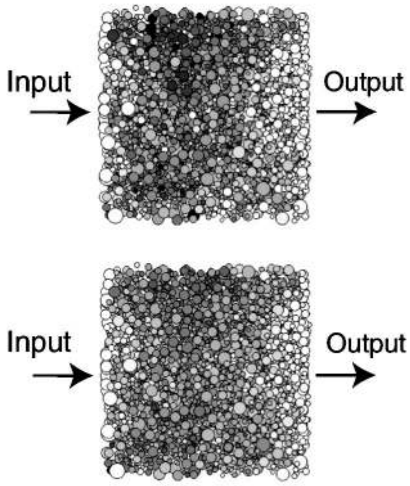

Fig. 16. Damage for: From top to bottom, ms2b, ms5b. Axial cuts.

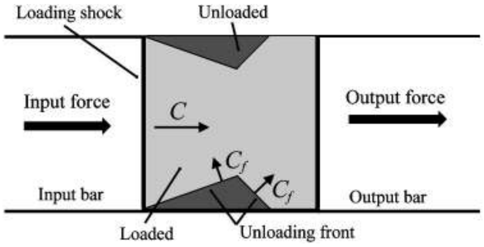

Fig. 17. Simplified lateral unloading process proposed for cylindrical specimen that fails by brittle fracture in split Hopkinson pressure bar compressional tests

than the compressive wave velocity. If this is the case, then the unloading could be sufficiently slow such that the central core of the specimen would not have had time to unload which means that this specimen will have a greater load-carrying capacity (see Fig. 17). Because of the fretting condition on the boundary, the unloading front from the free surface is not parallel to it, explaining the conelike shape of the damage distribution. All of these points are confirmed by the results of the tests simulations with the discrete element model.

Conclusions

A 3D DEM has proved its capability to model concrete. Quasi-static simulations of uniaxial compression and tension tests have been run to calibrate the model parameters, and to identify the numerical sample behavior.

First, the identification of the elastic behavior has been studied, and the results are qualitatively as well as quantitatively good. The stress state in the sample is consistent with laboratory results as well. Nonetheless, perturbations in the packing disorder have been found to strongly influence the values of Young's modulus and Poisson's coefficient, and high dispersions are observed. In order to reduce these dispersions, an energetic criterion has been introduced to modify the macro−micro constitutive equations of the model, which gives satisfactory results.

The method has proved its ability to capture the other characteristic properties of concrete: Quantitative results like peak strengths under both compression and tension and their associated strains, and fracture energy, as well as qualitative results like softening stress−strain relation in the postpeak region, and failure patterns, are in good accordance with laboratory results. Dispersions are higher than for elastic properties but are of the same order of magnitude as what experiments have shown.

Despite the great difficulty to reproduce such tests, SHPB dynamic compression experiments have been satisfactorily simulated, thus increasing the capability of the model. With the 3D discrete element model, the transient specimen state of damage and stress may be investigated and quite accurately represented. What is more, it proves able to quantitatively reproduce the increase of compressive strength with the increase of strain rate, and this, without requiring the use of viscosity in the model, or of any characteristic time. This confirms the inertia-based hypothesis: In other words, the increase of the dynamic strength in this range of strain rates is merely apparent and seems to be a structural effect.

SHPB tension tests are now being simulated to study the strain rate dependency under this type of loading. Then, steel-reinforced concrete structures under dynamic loading should be modeled.

Notation

The following symbols are used in this paper:

$\widetilde{A}_{\mathrm{int}}$ = average surface where an interaction is defined;
$\widetilde{A}^{nm}$ = average surface where an interaction between particles n and m;
C = celerity of the specimen's medium;
C_f = unloading velocity;
c = cohesion;
$D^{a,b}$ = D distance between centroids of two discrete elements a and b;

$D^{a,b}_{\mathrm{correction}}$ = correction distance for unloading;
$D^{a,b}_{\mathrm{eq}}$ = D_{eq} equilibrium distance between two discrete elements a and b;
$D_{\max}$ = maximum interaction distance;
E = Young's modulus;
E_{app} = apparent Young's modulus;
E_m = average Young's modulus;
E_{sc} = strain energy stored in the equivalent continuous medium;
E_{sd} = strain energy stored in the discrete assembly;
e = interaction coefficient;
$\mathbf{F}$ = interaction force vector;
$\mathbf{F}^{a \to b}$ = force from particle a on particle b;
$\mathbf{F}^n$ = normal interaction force vector;
$\mathbf{F}^s$ = shear interaction force vector;
$\mathbf{F}^s_{\mathrm{reduced}}$ = updated shear force vector during slip;
F_{input} = input force at the bar–specimen interface;
F_{output} = output force at the bar–specimen interface;
$F^n_{\max}$ = maximum normal force;
$F^s_{\max}$ = maximum shear force;
G_f = fracturation energy of the material;
I_a = set of particles in contact with particle a;
K^n = interaction normal stiffness;
K^s = interaction shear stiffness;
ℓ = length of the real specimen;
ℓ_{app} = apparent length of the numerical specimen;
$\mathbf{n}$ = unit interaction vector;
$\mathbf{n^{ab}}$ = unit interaction vector pointing from element a to element b;
R^a = R radius of a discrete element a;
S = cross-sectional area of the real specimen;
S_{app} = apparent cross-sectional area of the numerical specimen;
T = maximum tensile strength;
$\underline{U}^n$ = displacement of the element n;
V = homogenization volume;
V_{input} = input velocity at the bar–specimen interface;
V_{output} = output velocity at the bar–specimen interface;
$\mathbf{x}^a$ = $\mathbf{x}$ position vector of a discrete element a;
$\mathbf{x}^{a,b}$ = vector location of the interaction point between a and b;
$\dot{\mathbf{x}}$ = velocity vector of a discrete element;
$\ddot{\mathbf{x}}$ = acceleration vector of a discrete element;
x^a = component of the position vector of a discrete element a;
α = unloading factor;
β = softening factor;
γ = interaction range;
$\Delta\mathbf{F}^s$ = incremental interaction shear force vector;
$\Delta\mathbf{U}^s$ = shear displacement increment vector;
Δt = integration time step;
ε_i = strain of the longitudinal incident wave;
ε_r = strain of the longitudinal reflected wave;
ε_t = strain of the longitudinal transmitted wave;
$\underline{\underline{\varepsilon}}_c$ = strain matrix in the continuous medium;
$\underline{\underline{\varepsilon}}_d$ = strain matrix in the discrete medium;
$\dot{\varepsilon}$ = strain rate;
$\dot{\varepsilon}_s$ = average strain rate imposed on the specimen;
ν = Poisson's ratio;
ν_m = average Poisson's ratio;
ρ = density of the specimen;
σ_c = compressive strength;
σ_{cm} = average compressive strength;
σ_s = average stress imposed on the specimen;
σ_t = tensile strength;
σ_{tm} = average tensile strength;
$\underline{\underline{\sigma}}$ = stress matrix in the continuous medium;
$\underline{\underline{\sigma}}_d$ = stress matrix in the discrete medium;
ϕ_c = contact friction angle;
ϕ_i = internal friction angle; and
Ω_d = volume occupied by the assembly.

References

Allen, M., and Tildesley, D. (1987). Computer simulation of liquids.

Bardet, J.-P. (1997). "Introduction to computational granular mechanics." *Actes Du Colloque CISM*, Udine.

Bischoff, P., and Perry, S. (1991). "Compressive behavior of concrete at high strain rates." *Mater. Struct.,* 24, 425–450.

Brace, W. F., and Jones, A. H. (1971). "Comparison of uniaxial deformation in shock and static loading of three rocks." *J. Geophys. Res.,* 76, 4913–4921.

Cundall, P. (1988). "Formulation of a three-dimensional distinct element model. I: Scheme to detect and represent contacts in a system composed of many polyhedral blocks." *Int. J. Rock Mech. Min. Sci. Geomech. Abstr.,* 25(3), 107–116.

Cundall, P., and Strack, O. (1979). "Discrete numerical model for granular assemblies." *Geotechnique,* 29(1), 47–65.

Donzé, F.-V. (2000). *SDEC (Spherical Discrete Element Code), Version 2.00.* ⟨www.geonum.com⟩.

Donzé, F.-V. (2002). "Packing spherical discrete elements of unequal size." *Tech. Rep.* ISRN: GEONUM-NST-2002-02-FR+ENG. GEONUM report, France ⟨www.geonum.com⟩.

Donzé, F. V., Magnier, S. A., Daudeville, L., Mariotti, C., and Davenne, L. (1999). "Numerical study of compressive behavior of concrete at high strain rates." *J. Eng. Mech.,* 125(10), 1154–1163.

Dubé, J., Pijaudier-Cabot, G., and Laborderie, C. (1996). "Rate dependent damage model for concrete in dynamics." *J. Eng. Mech.,* 122(10), 939–947.

Gary, G. (1990). "Essais à grande vitesse sur béton. problèmes spécifiques." *Tech. Rep.* GRECO, Paris (in French).

Gopalaratnam, V., Gerstle, W., Isenberg, J., and Mindess, S. (1996). "State-of-the-art report on dynamic fracture." *Rep. No. 446*, American Concrete Institute Committee, Detroit.

Hart, R., Cundall, P., and Lemos, J. (1988). "Formulation of a three-dimensional distinct element model. II: Mechanical calculations for motion and interaction of a system composed of many polyhedral blocks." *Int. J. Rock Mech. Min. Sci. Geomech. Abstr.,* 25, 117–125.

Herrmann, H., Hansen, A., and Roux, S. (1989). "Fracture of disordered, elastic lattices in two dimensions." *Phys. Rev. B,* 39, 637–347.

Huang, H. (1999). "Discrete element modeling of tool-rock interaction." PhD thesis, Univ. of Minnesota.

Janach, W. (1976). "Role of bulking in brittle failure of rocks under rapid compression." *Int. J. Rock Mech. Min. Sci. Geomech. Abstr.,* 13, 177–186.

Jodrey, W., and Tory, E. (1985). "Computer simulation of close random packing of equal spheres." *Phys. Rev. A,* 32(4), 2347–2351.

Liao, C.-L., Chang, T.-P., and Young, D.-H. (1997). "Stress–strain relationship for granular materials based on the hypothesis of best fit." *Int. J. Solids Struct.,* 34(31–32), 4087–4100.

Magnier, S. A., Donze, F. V., and Mareschal, J.-C. (1997). "Discrete element project, rapport d'activités 1997, le code "spherical discrete element" SDEC et ses applications." *Internal Rep.* (in French).

Meguro, K., and Hakuno, M. (1989). "Fracture analyses of concrete structures by the modified distinct element method." *Struct. Eng./Earthquake Eng.,* 6(2), 283–294.

Moreau, J.-J. (1997). "Numerical investigation of shear zones in granular materials." *Friction, arching, contact dynamics*, P. Grassberger and D. Wolfs, eds. World Scientific, Singapore, 233–247.

Müller, D. (1996). ‘‘Techniques informatiques efficaces pour la simulation de milieux granulaires par des méthodes d'éléments distincts.’’ PhD thesis, Ecole polytechnique fédérale de Lausanne, Switzerland.

O'Connor, R. M. (1996). ‘‘A distributed discrete element modeling environment—algorithms, implementation, and applications.’’ PhD thesis, Massachussetts Institute of Technology, Cambridge, Mass.

Potyondy, D., Cundall, P., and Lee, C. (1996). ‘‘Modeling rock using bonded assemblies of circular particles.’’ *Rock Mech.,* 1937–1944.

Rossi, P., Mier, J. V., Boulay, C., and Maou, F. L. (1992). ‘‘The dynamic behavior of concrete: Influence of free water.’’ *Mater. Struct.,* 25, 509–514.

Rossi, P., Mier, J. G. V., Toutlemonde, F., Maou, F. L., and Boulay, C. (1994). ‘‘Effect of loading rate on the strength of concrete subjected to uniaxial tension.’’ *Mater. Struct.,* 27, 260–264.

Toutlemonde, F. (1995). ‘‘Résistance au choc des structures en béton; du comportement du matériau au calcul des ouvrages.’’ PhD thesis, Ecole Nationale des Ponts et Chaussées (in French).

Zhao, H., and Gary, G. (1996). ‘‘On the use of SHPB techniques to determine the dynamic behavior of materials in the range of small strains.’’ *Int. J. Solids Struct.,* 33(23), 3363–3375.